Journal of Biomolecular NMR (2022) 76:137–152
https://doi.org/10.1007/s10858-022-00401-4

ARTICLE

Measurement of $^{1}H^{\alpha}$ transverse relaxation rates in proteins: application to solvent PREs

Yuki Toyama[1,2,3] · Atul Kaushik Rangadurai[1,2,3,4] · Lewis E. Kay[1,2,3,4]

Received: 6 June 2022 / Accepted: 18 July 2022 / Published online: 26 August 2022

Abstract

It has recently been demonstrated that accurate near surface electrostatic potentials can be calculated for proteins from solvent paramagnetic relaxation enhancements (PREs) of amide protons measured using spin labels of similar structures but different charges (Yu *et al*. in Proc Natl Acad Sci 118(25):e2104020118, 2021). Here we develop methodology for extending such measurements to intrinsically disordered proteins at neutral pH where amide spectra are of very poor quality. Under these conditions it is shown that accurate PRE values can be measured using the haCONHA experiment that has been modified for recording $^{1}H^{\alpha}$ transverse relaxation rates. The optimal pulse scheme includes a spin-lock relaxation element for suppression of homonuclear scalar coupled evolution for all $^{1}H^{\alpha}$ protons, except those derived from Ser and Thr residues, and minimizes the radiation damping field from water magnetization that would otherwise increase measured relaxation rates. The robustness of the experiment is verified by developing a second approach using a band selective adiabatic decoupling scheme for suppression of scalar coupling modulations during $^{1}H^{\alpha}$ relaxation and showing that the measured PRE values from the two methods are in excellent agreement. The near surface electrostatic potential of a 103-residue construct comprising the C-terminal intrinsically disordered region of the RNA-binding protein CAPRIN1 is obtained at pH 5.5 using both $^{1}H^{N}$ and $^{1}H^{\alpha}$-based relaxation rates, and at pH 7.4 where only $^{1}H^{\alpha}$ rates can be quantified, with very good agreement between potentials obtained under all experimental conditions.

Keywords ^{1}H relaxation · Scalar coupled modulation · Intrinsically disordered proteins · CAPRIN1 · Electrostatic potential

Introduction

NMR spectroscopy is an extremely powerful technique for quantifying site-specific molecular dynamics (Mittermaier and Kay 2006; Palmer 2014; Anthis and Clore 2015). Most frequently this is accomplished through the measurement of heteronuclear (^{15}N, ^{13}C, ^{2}H, ^{31}P, ^{19}F) spin relaxation rates that can then be recast in terms of motional parameters in the context of a preferred model of dynamics (Lipari and Szabo 1982a, b). In this regard, the use of heteronuclear spins as probes of motion, as opposed to measurements involving ^{1}H spins, offers several advantages. Importantly, it is often the case that the relaxation of heteronuclei can be quantitatively analyzed in terms of a small number of well-defined interactions, greatly simplifying data analysis. An example is the popular series of ^{15}N R_1, R_2, and heteronuclear NOE experiments where a relatively simple two-spin ^{15}N–$^{1}H^{N}$ spin system is sufficient to describe the experiments (Kay et al. 1989). The situation is more complex for ^{13}C, as coupled relaxation between spin interactions, such as ^{13}C–^{1}H dipolar pairs in methylene and methyl groups (Vold and Vold 1976; Werbelow and Grant 1977), complicates the analysis (Kay and Torchia 1991), as does scalar coupling and relaxation between proximal ^{13}C spins in uniformly ^{13}C labeled samples (Yamazaki et al. 1994). The development of labeling schemes involving the placement of isolated ^{13}C spins in the system of interest (Goto et al. 1999; Kainosho et al.

✉ Yuki Toyama
yuki.toyama@utoronto.ca

✉ Lewis E. Kay
kay@pound.med.utoronto.ca

1 Department of Molecular Genetics, University of Toronto, Toronto M5S 1A8, Canada

2 Department of Chemistry, University of Toronto, Toronto, ON M5S 3H6, Canada

3 Department of Biochemistry, University of Toronto, Toronto, ON M5S 1A8, Canada

4 Program in Molecular Medicine, Hospital for Sick Children Research Institute, Toronto, ON M5G 0A4, Canada

2006; Teilum et al. 2006; Lundström et al. 2007; Kasinath et al. 2013), in concert with the substitution of protons with deuterons (Ishima et al. 1999; Tugarinov and Kay 2005), can simplify the spin system so that it is well approximated as a two-spin ^{13}C–^{1}H pair. In some cases experiments are relatively benign to the effects of scalar couplings that manifest in uniformly ^{13}C labeled molecules, such as carbon-13 CEST (Vallurupalli et al. 2013), for example, while special pulse schemes have been developed for mitigating the effects of the homonuclear ^{13}C couplings in ^{13}C relaxation measurements (Yamazaki et al. 1994). Other applications exploit the inherent complexity that is introduced by the multiplicity of interactions within methylene and methyl groups to obtain additional insights into dynamics using experiments that rely on cross-correlated relaxation (Sun et al. 2011; Tugarinov and Clore 2021). Measuring ^{2}H spin relaxation (Muhandiram et al. 1995) is advantageous in that the decay is dominated by the quadrupolar interaction, and the obtained rates can be cross-validated by recording as many as five independent decay times for each deuteron (Millet et al. 2002). A limitation is that the experiments are less sensitive than those quantifying ^{15}N and, often, ^{13}C relaxation, so that applications are largely focused on methyl groups (Kay et al. 1998).

Far fewer biomolecular applications involving ^{1}H relaxation have appeared in the literature, reflecting the fact that ^{1}H spins are most often both dipolar and scalar coupled to neighboring protons in fully protonated molecules, leading to the facile transfer of magnetization between protons and, therefore, contaminating measured relaxation rates. Labeling strategies involving partial deuteration are helpful in this regard, producing isolated ^{1}H spins at significant numbers of backbone and sidechain positions (Lundström et al. 2009; Hansen et al. 2012). However, it remains of interest to establish robust methods for measurement of relaxation rates in fully protonated proteins, in particular focusing on backbone ^{1}H$^{\alpha}$ spins, which is the subject matter of this report. Our interest in the measurement of ^{1}H$^{\alpha}$ relaxation rates concerns quantification of solvent paramagnetic relaxation enhancements (PREs) in an attempt to map near surface electrostatic potentials (Yu et al. 2021) in intrinsically disordered proteins (IDPs). As PRE effects scale with the square of the gyromagnetic ratios of the probe spins (Abragam 1961), there are clear advantages to proton-based experiments. The obvious choice is to record ^{15}N–^{1}H^{N} HSQC spectra that measure ^{1}H^{N} rates, as these can be faithfully obtained via simple spin-echo schemes in which evolution from ^{1}H^{N}–^{1}H scalar couplings is refocused by the application of an ^{1}H^{N}-selective pulse in the center of a relaxation period (Donaldson et al. 2001). Alternatively, the effects of ^{1}H^{N}–^{1}H *J*-modulation can be "removed" during analysis of spectra recorded with non-selective ^{1}H^{N} chemical shift refocusing pulses by using identical relaxation times for both paramagnetic and diamagnetic samples and fitting paramagnetic relaxation rates directly from intensity ratios of corresponding peaks in the resulting pairs of spectra (Iwahara et al. 2004, 2007). Yet in some applications, especially those involving IDPs or intrinsically disordered regions (IDRs) in otherwise folded molecules that must be performed at neutral pH, amide spectra are severely compromised due to rapid hydrogen exchange. In these cases an approach that circumvents both the recording of ^{1}H^{N} chemical shifts and measurement of ^{1}H^{N} relaxation rates, that are likely to be contaminated by exchange with water, complicating extraction of robust exchange rates, would be preferred. Herein we develop a pseudo-4D experiment for measurement of ^{1}H$^{\alpha}$ relaxation rates based on the haCONHA pulse scheme that records (^{13}CO$_i$,^{15}N$_{i+1}$,^{1}H$^{\alpha}_{i}$) correlations, where the chemical shifts of ^{13}CO and ^{1}H$^{\alpha}$ spins of residue i are correlated with the ^{15}N spin of the subsequent residue, $i+1$ (Mäntylahti et al. 2011; Wong et al. 2020a). Important considerations for the design and optimization of the pulse scheme are described, along with applications to the C-terminal region of the RNA binding protein CAPRIN1 (Kedersha et al. 2016; Nakayama et al. 2017), so as to establish the robustness of the approach and its utility in studies of IDPs at neutral pH values and higher.

Material and methods

Sample preparation

The C-terminal region of CAPRIN1 (residues 607–709, Uniprot: Q14444) was expressed and purified as described previously (Kim et al. 2019; Wong et al. 2020a). As reported in our previous study (Wong et al. 2020a), residues N623-G624 and N630-G631 slowly form isoaspartate (IsoAsp)-Gly peptide linkages over time. As the formation of IsoAsp can alter the charge distribution of the CAPRIN1 molecule, N623T and N630T double mutations were introduced; the double Thr mutant was used in all of the experiments (and is referred to as CAPRIN1 in the discussion which follows). These mutations were introduced by using Quikchange site-directed mutagenesis (Agilent). Uniformly ^{13}C, ^{15}N-labeled CAPRIN1 was produced by bacterial growth, with expression using minimal media supplemented with [U-^{13}C]-glucose and $^{15}NH_4Cl$ as the sole carbon and nitrogen sources, respectively. The NMR samples were comprised of 280–300 µM U-^{13}C,^{15}N CAPRIN1, 25 mM MES-NaOH (pH 5.5) or 25 mM HEPES–NaOH (pH 7.4), and 3% D_2O. For solvent PRE measurements, 3-carboxy-PROXYL (Sigma-Aldrich) or 3-carbamoyl-PROXYL (Sigma-Aldrich) was added to a final concentration of 5 mM from a ~ 100 mM stock solution. The concentration of the paramagnetic co-solutes in the stock solution was measured by ^{1}H 1D NMR

after reducing the spin-label, using a procedure established by Iwahara and co-workers (Yu et al. 2021).

NMR measurements

All NMR measurements were performed at 23.5 Tesla (1 GHz ^{1}H frequency) on a Bruker Avance Neo spectrometer or at 14.0 Tesla (600 MHz ^{1}H frequency) on a Bruker Avance III HD spectrometer, equipped with cryogenically cooled *x*, *y*, *z* pulsed-field gradient triple-resonance probes. All spectra were processed and analyzed using the NMRPipe suite of programs (Delaglio et al. 1995) and visualized using the Python package nmrglue (Helmus and Jaroniec 2013). Peak intensities were extracted either by using the Peakipy software package (https://github.com/j-brady/peakipy) for 2D datasets, or by analyzing the time-domains of pseudo-4D datasets (haCONHA of Fig. 1A.1 or A.3), as described previously (Long et al. 2015; Wong et al. 2020b). In time-doming fitting, the reference 3D spectrum recorded with the first relaxation delay was reconstructed using SMILE (Ying et al. 2017), and the peak list required for the time-domain fitting was obtained by analyzing the processed data.

^{1}H$^\alpha$ R_2 or ^{1}H$^\alpha$–^{13}C$^\alpha$ longitudinal order relaxation measurements were recorded with pulse schemes that are based on the haCONHA experiment (Wong et al. 2020a) (see Fig. 1), and were performed in a pseudo-4D manner where the indirect ^{13}CO and ^{15}N dimensions were non-uniformly sampled using a Poisson-gap sampling schedule (Hyberts et al. 2010) (^{1}H$^\alpha$ R_2, measured using the schemes of Fig. 1A.1 or A.3) or by measuring 2D ^{13}CO–^{1}H$^\alpha$ or ^{15}N–^{1}H$^\alpha$ planes (^{1}H$^\alpha$ R_2, measured by the adiabatic scheme of Fig. 1A.2; $2I_z^\alpha C_z^\alpha$ longitudinal order relaxation using the scheme shown schematically in Fig. 3B that replaces A in Fig. 1). Measurements were performed at 600 MHz and 25 °C with relaxation delays set to 0, 4, 8, 12, 16, 20, 25, and 30 ms for the scheme of Fig. 1A.1 and A.3, or 0–40 ms, in 8 ms steps, for the scheme of Fig. 1A.2. Longitudinal order decay rates were quantified with delays of 0, 4, 8, 12, 16, 20, 25, and 30 ms.

^{1}H^N R_2 relaxation measurements (pH 5.5 sample) were performed using a transverse relaxation-optimized spectroscopy (TROSY) scheme (Pervushin et al. 1997), with a ^{1}H spin-echo variable delay interval inserted immediately prior to direct detection. A selective REBURP pulse (Geen and Freeman 1991) (length of 1800 µs and centered at 7.7 ppm, 1 GHz) during the ^{1}H spin-echo period refocuses homonuclear *J*-evolution of ^{1}H^N spins. The measurements were performed at 1 GHz and 25 °C, with relaxation delays of 2, 4, 6, 8, 12, 16, 22, and 30 ms.

Fitting of ^{1}H$^\alpha$ and ^{1}H^N relaxation rates

^{1}H$^\alpha$ PREs were quantified by fitting intensity ratios of corresponding peaks in the "paramagnetic" (with 5 mM 3-carboxy-PROXYL or 5 mM 3-carbamoyl-PROXYL, denoted by − or *N*, respectively) and "diamagnetic" (no PRE co-solute molecules) experiments to the single exponential decay function,

$$\frac{I^{para.,i}(T_{relax})}{I^{dia.}(T_{relax})} = exp(-\Gamma_{2,i}T_{relax}) \quad (1)$$

where $I^{para.,i}(T_{relax})$ and $I^{dia.}(T_{relax})$ are signal intensities at time T_{relax} for peaks in the paramagnetic and diamagnetic samples, and $\Gamma_{2,i}$ is the PRE contribution to the ^{1}H$^\alpha$ R_2 rate ($i \in \{-, N\}$). As described by Iwahara, Clore and co-workers (Iwahara et al. 2004, 2007; Yu et al. 2022), by taking the ratio of intensities it is possible to divide out contributions from ^{1}H–^{1}H *J*-modulations that would otherwise contaminate the relaxation rates. Nevertheless, scalar-coupled evolution does attenuate the signals so that it is highly desirable to suppress the modulations in the first place, and this is possible for ^{1}H$^\alpha$ spins from all residues with the exception of Ser and Thr, as described in detail below. We have also observed that for a number of non-Ser/Thr residues there is a slight deviation from single exponential decay, presumably because of modulation from couplings that are not completely suppressed by the 1 kHz spin-lock field of Fig. 1A.1 that selectively locks ^{1}H$^\alpha$ magnetization. Use of Eq. (1) is beneficial for these cases as well.

^{1}H^N PREs are quantified by fitting the decay of signals to a single exponential function to obtain $R_2^{para.,i}$ and $R_2^{dia.}$ rates, from which the PRE contribution is calculated as $\Gamma_{2,i} = R_2^{para.,i} - R_2^{dia.}$. Fits made use of in-house written programs (Python 3.7), exploiting the Levenberg–Marquardt algorithm of the Lmfit python software package (https://lmfit.github.io/lmfit-py/).

Calculations of near-surface electrostatic potentials

Near-surface electrostatic potentials were calculated from the PRE rates obtained with 3-carboxy-PROXYL ($\Gamma_{2,-}$) and 3-carbamoyl-PROXYL ($\Gamma_{2,N}$) derivatives using the following equation, as described previously (Yu et al. 2021),

$$\phi_{ENS} = -\frac{k_B T}{e}\ln\left(\frac{\Gamma_{2,N}}{\Gamma_{2,-}}\right) \quad (2)$$

where k_B is Boltzmann's constant (8.62×10^{-5} eV/K), T is temperature (298.15 K), and e is the charge of an electron. Note that the denominator was set to 1e as the difference in charge between 3-carboxy-PROXYL and 3-carbamoyl-PROXYL is 1. In the calculations, residues with $\Gamma_{2,-}$ or $\Gamma_{2,N}$ larger than 0.5 s^{-1} were used.

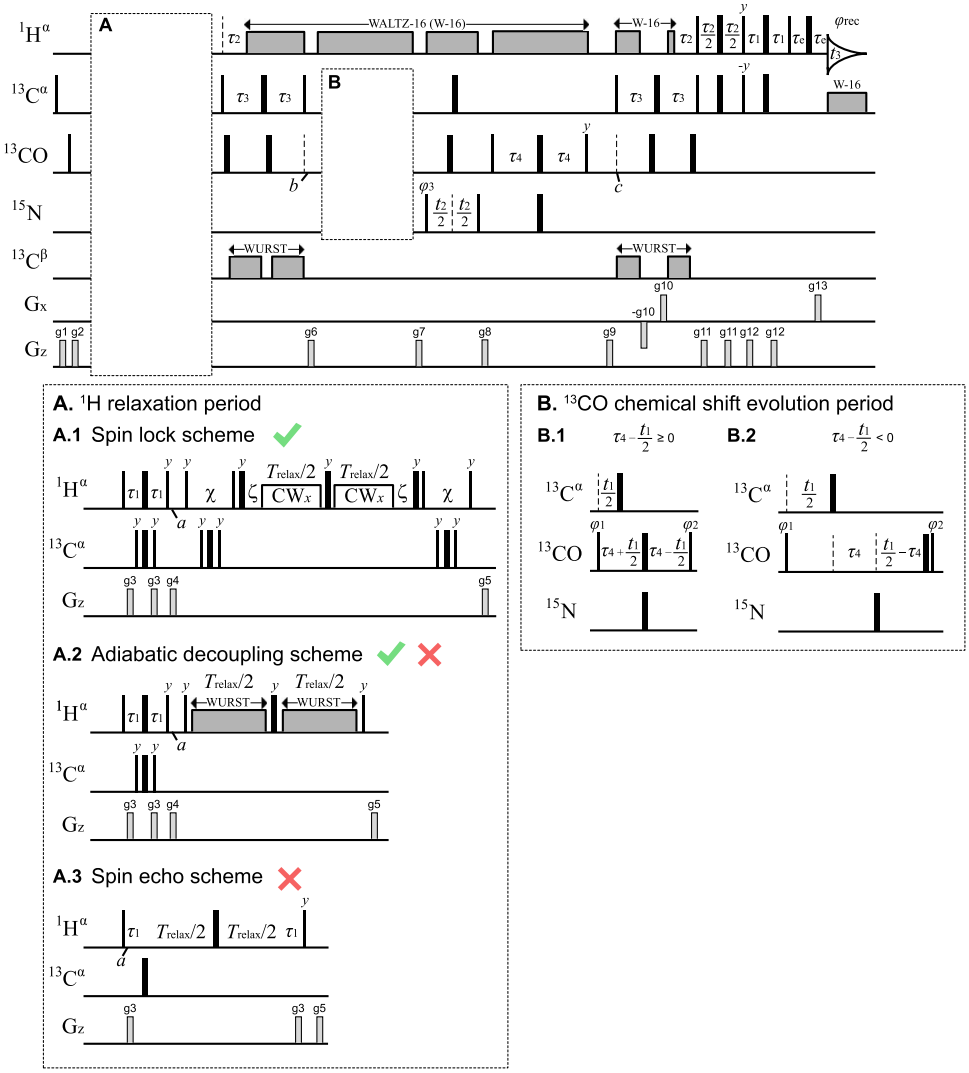

Simulations of $^{1}H^{\alpha}$ scalar coupled evolution with and without a spin-locking field

The scalar-coupled evolution of $^{1}H^{\alpha}$ magnetization was simulated by calculating the time-evolution of the density matrix (Sørensen et al. 1984). The operative Hamiltonian ($\hat{\mathcal{H}}_0$) is composed of chemical shift ($\hat{\mathcal{H}}_{CS}$), scalar coupling ($\hat{\mathcal{H}}_J$), and spin-lock field ($\hat{\mathcal{H}}_{SL}$) terms, as follows,

$$\hat{\mathcal{H}}_0 = \hat{\mathcal{H}}_{CS} + \hat{\mathcal{H}}_J + \hat{\mathcal{H}}_{SL} = \sum_i \Omega_i I_z^i + \sum_{i \neq j} 2\pi J_{ij} \boldsymbol{I}^i \cdot \boldsymbol{I}^j + \sum_i \omega_1 I_x^i \quad (3)$$

where Ω_i is the offset frequency (rad/sec) of proton spin i from the radio frequency carrier, I_x and I_z denote the x and z components of ^{1}H spin angular momentum, respectively, J_{ij} is the homonuclear scalar coupling constant between spins i j, ω_1 is the ^{1}H spin-lock field strength in rad/sec ($1000 \times 2\pi$ rad/sec was used in experiments), and it is understood that only one of the terms of the form $2\pi J_{\alpha\beta 1} \boldsymbol{I}^{\alpha} \cdot \boldsymbol{I}^{\beta 1}$ or $2\pi J_{\beta 1 \alpha} \boldsymbol{I}^{\beta 1} \cdot \boldsymbol{I}^{\alpha}$ is included, for example. The number of spins, and the chemical shifts and J coupling constants used in each simulation are indicated in the schematics of Fig. 2. In the calculations, only 2-bond or 3-bond homonuclear J couplings were considered and heteronuclear couplings were not included. In the case of a "typical amino-acid", such as shown in Fig. 2A (top left), for example, a set of 4 spins $i,j \in \{\alpha, \beta^1, \beta^2, H^N\}$ was considered. Relaxation was not included in the simulations. The time evolution of the density matrix, evolving with the scheme of Fig. 2A (top right), was calculated by numerically solving the Liouville von-Neumann equation,

◂**Fig. 1** The haCONHA pulse sequence for measuring $^{1}H^{\alpha}$ R_2 rates by observing ($^{13}CO_i$,$^{15}N_{i+1}$,$^{1}H^{\alpha}_i$) correlations. Many of the details of the pulse scheme are as described previously (Wong et al. 2020a); however, for completeness they are repeated here. All 90° (180°) rectangular pulses are denoted by narrow (wide) bars and applied along the *x*-axis unless otherwise indicated. The ^{1}H carrier is on resonance with the water line (~4.7 ppm), the ^{13}C carrier is at 176 ppm between points *b* and *c* and otherwise at 58 ppm, and the ^{15}N carrier is at 119 ppm (but see below for specific details about each of the schemes in panel **A**). ^{1}H WALTZ-16 decoupling is applied with a field of ~6.25 kHz. $^{13}C^{\alpha}$ and ^{13}CO 90° and 180° rectangular pulses are applied with fields of $\Delta\Omega/\sqrt{15}$ and $\Delta\Omega/\sqrt{3}$, respectively, where $\Delta\Omega = 118$ ppm, ensuring minimal excitation of ^{13}CO spins when $^{13}C^{\alpha}$ pulses are applied and vice versa (Kay et al. 1990). $^{13}C^{\alpha}$ WALTZ-16 decoupling during t_3 acquisition uses a field of ~2 kHz (600 MHz spectrometer). Inset A shows three approaches for measuring $^{1}H^{\alpha}$ R_2 rates, including (i) application of a ^{1}H spin lock (A.1), (ii) application of $^{1}H^{\beta}$, $^{1}H^{N}$ adiabatic decoupling (A.2), and a spin-echo scheme (A.3). In scheme A.1 the ^{1}H and ^{13}C carriers are placed at 4.35 ppm and 50 ppm, respectively, with the placement of the ^{13}C carrier so as to reduce off-resonance effects for $^{13}C^{\alpha}$ of Gly. The ^{1}H spin-lock is achieved with a 1 kHz CW field along *x*, at the center of which a high power 180_y pulse is applied. Prior to the spin-lock, ^{1}H spins are aligned along their effective fields via a pulse/delay scheme, described previously (Hansen and Kay 2007), where χ and ζ are set to $1/\omega_{SL} - (4/\pi)$pw and $(2/\pi)$pw, respectively, where ω_{SL} is the RF field strength for the ^{1}H spin-lock and pw is the ^{1}H high power 90° pulse width. The relaxation delay, T_{relax}, was varied from 0 to 30 ms. In scheme A.2, selective ^{1}H decoupling is achieved using a constant adiabaticity WURST decoupling element (Kupce and Wagner 1996) swept from 1.1 to 3.3 ppm (8 ms WURST (Kupce and Freeman 1995) pulse width) centered at 2.2 pm, a typical $^{1}H^{\beta}$ shift value, along with a second field swept from 7.4 to 8.6 ppm centered on the amide $^{1}H^{N}$ protons. T_{relax} was varied from 0 to 40 ms in 8 ms spacing intervals so as to be synchronous with the ^{1}H decoupling sequence. The delays are: $\tau_1 = 1.7$ ms, $\tau_3 = 4.5$ ms, $\tau_4 = 15$ ms, with τ_e sufficiently long to accommodate gradient g13. The delay τ_2 is set to 2.3 ms, a compromise so as to obtain cross peaks from all residues including Gly. $^{13}C^{\beta}$ decoupling is achieved using a constant adiabaticity WURST decoupling element swept from 41 to 15 ppm (5 ms WURST pulse width), along with a second field swept from 68 to 72 ppm. ^{13}CO chemical shift evolution during t_1 is acquired in a semi-constant time mode (Grzesiek et al. 1993; Logan et al. 1993) as depicted in **B**. The phase cycle used is: $\varphi_1 = 2(x),2(-x)$; $\varphi_2 = y + 48.5°$ (600 MHz); $\varphi_3 = x,-x$; and $\varphi_{rec} = x,2(-x),x$. The phase change applied to φ_2 corrects for the Bloch-Siegert shift caused by application of the uncompensated $^{13}C^{\alpha}$ pulse during the t_1 period. Quadrature detection in t_1 and t_2 is achieved by STATES-TPPI (Marion et al. 1989) of φ_1 and φ_3, respectively. Gradients are applied with the following durations (ms) and strengths (in % maximum): g1: (0.5, 24%), g2: (1.0, 24%), g3: (0.256, 15%), g4: (0.5, 52.8%), g5: (1.0, 40%), g6: (1.25, 80%), g7: (1.5, 80%), g8: (0.9, 50%), g9: (1.0, 15%), g10: (0.512, 90%), g11: (0.4, 40%), g12: (0.3, 15%), g13: (0.256, 90.3%)

$$\begin{aligned} \sigma(T_{relax}) &= U\sigma(0)U^{-1} \\ U &= \exp\left(-i\hat{\mathcal{H}}_0\frac{T_{relax}}{2}\right)\exp(-i\pi\textstyle\sum_i I_y^i)\exp\left(-i\hat{\mathcal{H}}_0\frac{T_{relax}}{2}\right) \\ U^{-1} &= \exp\left(i\hat{\mathcal{H}}_0\frac{T_{relax}}{2}\right)\exp(i\pi\textstyle\sum_i I_y^i)\exp\left(i\hat{\mathcal{H}}_0\frac{T_{relax}}{2}\right) \end{aligned} \quad (4)$$

with $\sigma(0) = I_x^{\alpha}$ (in-phase $^{1}H^{\alpha}$ magnetization). Terms from other spins were set to zero initially. Note that, experimentally, the proton magnetization of interest during the relaxation period is antiphase with respect to the attached ^{13}C spin ($2I_x^{\alpha}C_z^{\alpha}$, see Fig. 1) and other transverse magnetization components coupled to $^{13}C^{\alpha}$ (such as $2I_x^{\beta}C_z^{\alpha}$) are not present at the beginning of this period. Thus, when considering a homonuclear spin system exclusively, the analogous situation is one where initial magnetization components with the exception of I_x^{α} are set to 0. The expectation value of the *x*-transverse magnetization at time T_{relax} ($M(T_{relax})$) was calculated by taking the trace of the product of $\sigma(T_{relax})$ and I_x^{α}. $M(T_{relax})$ profiles for $0 \le T_{relax} \le 30$ ms, with a time step of 1 ms, were calculated from

$$M(T_{relax}) = \frac{\mathrm{tr}\{\sigma(T_{relax}) \cdot I_x^{\alpha}\}}{\mathrm{tr}\left\{\left(I_x^{\alpha}\right)^{\dagger} \cdot I_x^{\alpha}\right\}} \quad (5)$$

and plotted in Fig. 2A, B.

Simulating the effects of cross-relaxation

As described in the text, a spin-lock field has been used to minimize evolution of magnetization due to homonuclear scalar couplings. We wondered whether dipolar cross-relaxation between neighboring spins would become an issue (ROE effect) under these conditions, leading to non-exponential decay of $^{1}H^{\alpha}$ magnetization and to mixing of PREs from proximal ^{1}H spins. We have, therefore, simulated an *I-C-M* three spin system, where *I*, *C*, and *M* are $^{1}H^{\alpha}$, $^{13}C^{\alpha}$, and $^{1}H^{\beta}$ spins, respectively, considering relaxation and scalar coupled evolution. In principle, a complete description of this spin system requires a basis of 64 elements. However, as C_z is the only ^{13}C operator considered (^{13}C pulses are not applied), a reduced basis set suffices, composed of 30 elements (excluding the identity operator). The normalized basis set can be expressed by using a column vector with

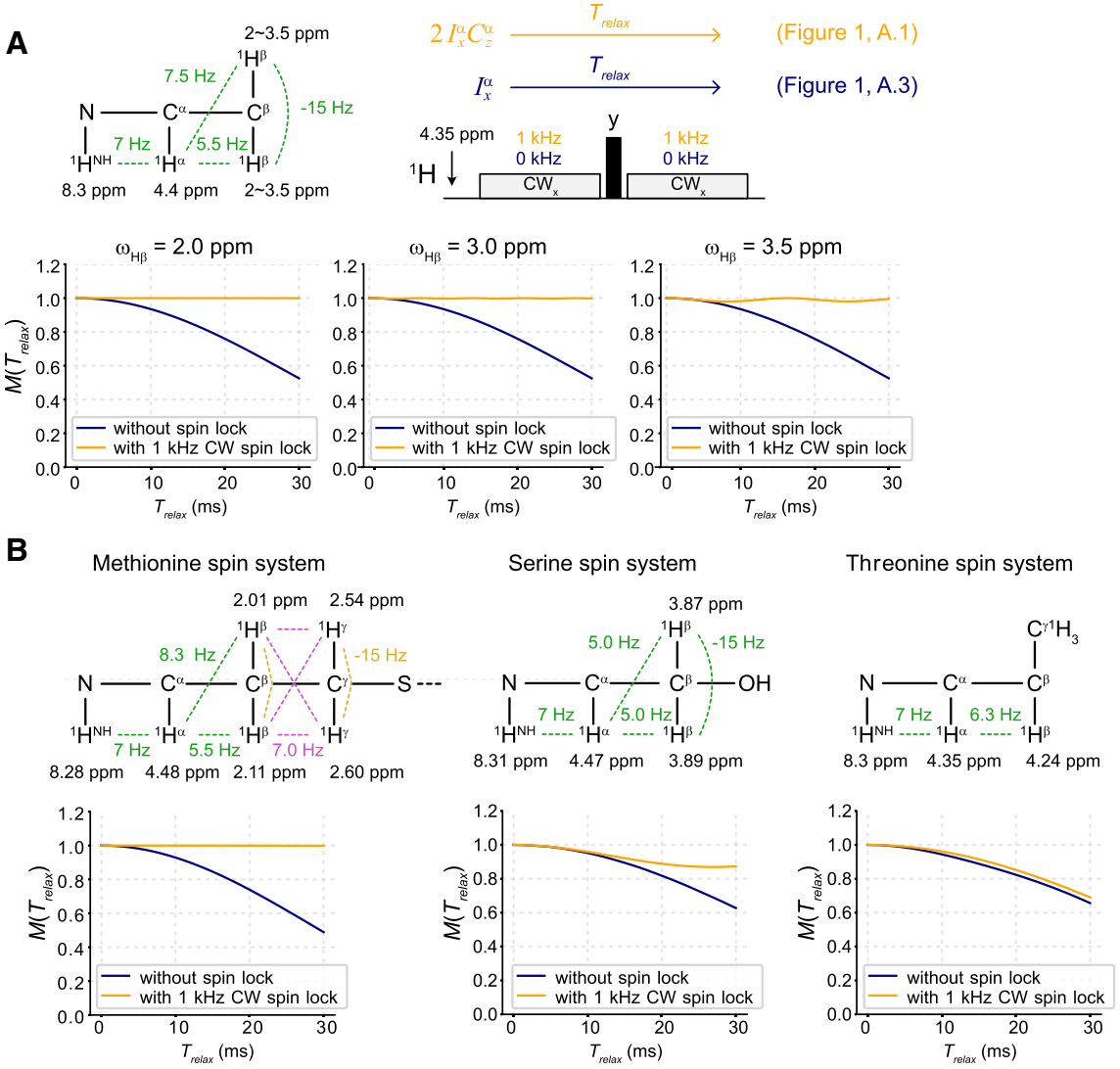

Fig. 2 Simulating the evolution of $^1H^\alpha$ magnetization due to $^1H^\alpha$-^1H scalar couplings. **A** Evolution of $^1H^\alpha$ magnetization in a spin system typical for amino acids, where $^1H^N$ and two $^1H^\beta$ protons are scalar-coupled to $^1H^\alpha$. (top left) The chemical shifts of each spin and the *J*-coupling constants used are shown. (top right) Pulse scheme elements, similar to those used in experiments of Fig. 1A.1 (orange; $^1H^\alpha$ magnetization, $2I_x^\alpha C_z^\alpha$, is locked along its effective field at the start of the spin-lock, as is done experimentally) and in 1A.3 (navy, starting from I_x^α). (bottom) Plots of the trajectories of $^1H^\alpha$ *x*-magnetization calculated with different $^1H^\beta$ chemical shifts (left: 2 ppm, center: 3 ppm, and right: 3.5 ppm), in the presence (orange) and absence (navy) of a 1 kHz spin-lock field centered at 4.35 ppm. **B** Evolution of $^1H^\alpha$ magnetization in methionine (left), serine (center), and threonine (right) spin systems. (top) The chemical shifts of each spin and the *J*-coupling constants are shown. (bottom) Trajectories of calculated $^1H^\alpha$ *x*-magnetization with (orange) and without (navy) a 1 kHz spin-lock field centered at 4.35 ppm. The chemical shifts of each ^1H spin were taken from a tabulation of random coil values (Wishart et al. 1995) and the *J*-coupling constants were set to those measured in unfolded proteins (Hähnke et al. 2010) or those typically observed in folded proteins

30 Cartesian product operators (Ernst et al. 1987; Allard et al. 1998),

$$\sigma = [I_x, I_y, I_z, M_x, M_y, M_z, 2I_xM_z, 2I_yM_z, 2I_zM_x, 2I_zM_y, 2I_xM_x, 2I_xM_y, 2I_yM_x, 2I_yM_y, 2I_zM_z, 2I_xC_z, 2I_yC_z, 2I_zC_z, \cdots, 4I_xM_zC_z, \cdots, 4I_zM_zC_z]^+ \quad (6)$$

where $^+$ denotes the transpose operation.

The operative Hamiltonian in this case is,

$$\hat{\mathcal{H}} = \Omega_I I_z + \Omega_M M_z + 2\pi J_{IM} \boldsymbol{I} \cdot \boldsymbol{M} + 2\pi J_{IC} I_z C_z + \omega_1 (I_x + M_x) \quad (7)$$

where Ω_I and Ω_M are the offsets of ^{1}H spins I and M from the ^{1}H carrier, J_{IM} and J_{IC} are I-M and I-C homo- and hetero-nuclear scalar coupling constants, respectively, and ω_1 ($1000 \times 2\pi$ rad/sec) is the strength of an applied field on spins I and M. In all simulations, $J_{IM} = 7$ Hz, $J_{IC} = 140$ Hz and a static magnetic field of 14.0 Tesla (600 MHz ^{1}H resonance frequency) was used.

The evolution of the density matrix, σ, during the scheme of Fig. 2A (top right) was calculated by numerically solving

$$\sigma(T_{relax}) = \exp\{-\left(i\hat{\hat{\mathcal{L}}} + \hat{\hat{\mathcal{R}}}\right)\frac{T_{relax}}{2}\}\hat{\hat{U}}^{y,\pi}\exp\{-\left(i\hat{\hat{\mathcal{L}}} + \hat{\hat{\mathcal{R}}}\right)\frac{T_{relax}}{2}\}\sigma(0) \quad (8)$$

In Eq. (8) $\hat{\hat{\mathcal{L}}}$ is a 30×30 Liouvillian matrix that includes J and chemical shift evolution, $\hat{\hat{\mathcal{R}}}$ is a relaxation matrix, including auto- and cross-relaxation terms, and $\hat{\hat{U}}^{y,\pi}$ is a rotation matrix that "applies" a ^{1}H 180° pulse along y in the center of the spin lock element. Each component of $\hat{\hat{\mathcal{L}}}$ and $\hat{\hat{U}}^{y,\pi}$ was calculated as

$$\hat{\hat{\mathcal{L}}}_{rs} = \frac{\langle r|[\hat{\mathcal{H}}, s]\rangle}{\langle r|r\rangle} \quad (9)$$

$$\hat{\hat{U}}^{y,\pi}_{rs} = \frac{\langle r|[\exp(-i\pi(I_y + M_y))s\exp(i\pi(I_y + M_y))]\rangle}{\langle r|r\rangle} \quad (10)$$

where $|r>$ and $|s>$ are density elements listed in Eq. (6).

The relaxation matrix, $\hat{\hat{\mathcal{R}}}$, includes auto-relaxation terms for each operator and cross-relaxation terms coupling $I_x \leftrightarrow M_x$, $I_y \leftrightarrow M_y$, $I_z \leftrightarrow M_z$, $2I_xM_z \leftrightarrow 2I_zM_x$, $2I_yM_z \leftrightarrow 2I_zM_y$, $2I_xM_y \leftrightarrow 2I_yM_x$, $2I_xC_z \leftrightarrow 2M_xC_z$, $2I_yC_z \leftrightarrow 2M_yC_z$, $2I_zC_z \leftrightarrow 2M_zC_z$, $4I_xM_zC_z \leftrightarrow 4I_zM_xC_z$, $4I_yM_zC_z \leftrightarrow 4I_zM_yC_z$, and $4I_xM_yC_z \leftrightarrow 4I_yM_xC_z$. Auto-relaxation was calculated by including ^{1}H-^{1}H dipolar interactions between each of spins I and M and a pair of external proton spins (one unique external ^{1}H for each of I and M; $r_{HH,ext} = 2.1$ Å for both I and M spins), ^{1}H-^{1}H dipolar interactions between spins I and M ($r_{HH,IM} = 1.9$ Å), and ^{1}H-^{13}C dipolar interactions between spins I and M and their directly bonded ^{13}C nuclei ($r_{CH} = 1.1$ Å). Only terms proportional to the spectral density evaluated at zero frequency are included in our analysis. Although a separate carbon spin one-bond coupled to spin M is not explicitly included in the spin system under consideration (Eq. (6)), we have, nevertheless, included a C-M dipolar interaction that would normally be present in the U-^{13}C,^{15}N proteins that are studied experimentally. The relaxation matrix can, thus, be defined as follows (Allard et al. 1997),

$$\hat{\hat{R}} = \left[\begin{array}{c|c} R^* & 0 \\ \hline 0 & R^* \end{array}\right]$$

$$R^* = \begin{bmatrix}
R_{11} & 0 & 0 & \sigma_{ROE} & 0 & 0 & 0 & 0 & 0 & 0 & 0 & 0 & 0 & 0 & 0 \\
0 & R_{22} & 0 & 0 & \sigma_{ROE} & 0 & 0 & 0 & 0 & 0 & 0 & 0 & 0 & 0 & 0 \\
0 & 0 & R_{33} & 0 & 0 & \sigma_{NOE} & 0 & 0 & 0 & 0 & 0 & 0 & 0 & 0 & 0 \\
\sigma_{ROE} & 0 & 0 & R_{44} & 0 & 0 & 0 & 0 & 0 & 0 & 0 & 0 & 0 & 0 & 0 \\
0 & \sigma_{ROE} & 0 & 0 & R_{55} & 0 & 0 & 0 & 0 & 0 & 0 & 0 & 0 & 0 & 0 \\
0 & 0 & \sigma_{NOE} & 0 & 0 & R_{66} & 0 & 0 & 0 & 0 & 0 & 0 & 0 & 0 & 0 \\
0 & 0 & 0 & 0 & 0 & 0 & R_{77} & 0 & R_{79} & 0 & 0 & 0 & 0 & 0 & 0 \\
0 & 0 & 0 & 0 & 0 & 0 & 0 & R_{88} & 0 & R_{810} & 0 & 0 & 0 & 0 & 0 \\
0 & 0 & 0 & 0 & 0 & 0 & R_{97} & 0 & R_{99} & 0 & 0 & 0 & 0 & 0 & 0 \\
0 & 0 & 0 & 0 & 0 & 0 & 0 & R_{108} & 0 & R_{1010} & 0 & 0 & 0 & 0 & 0 \\
0 & 0 & 0 & 0 & 0 & 0 & 0 & 0 & 0 & 0 & R_{1111} & 0 & 0 & 0 & 0 \\
0 & 0 & 0 & 0 & 0 & 0 & 0 & 0 & 0 & 0 & 0 & R_{1212} & R_{1213} & 0 & 0 \\
0 & 0 & 0 & 0 & 0 & 0 & 0 & 0 & 0 & 0 & 0 & R_{1312} & R_{1313} & 0 & 0 \\
0 & 0 & 0 & 0 & 0 & 0 & 0 & 0 & 0 & 0 & 0 & 0 & 0 & R_{1414} & 0 \\
0 & 0 & 0 & 0 & 0 & 0 & 0 & 0 & 0 & 0 & 0 & 0 & 0 & 0 & R_{1515}
\end{bmatrix} \quad (11)$$

The auto-relaxation rates (R_{11}–R_{1515}), anti-phase and multiple-quantum cross-relaxation terms (R_{79}, R_{97}, R_{810}, R_{108}, R_{1213} and R_{1312}) are given by Desvaux et al. (1994) and Allard et al. (1997)

$$
\begin{aligned}
&R_{11} = R_{22} = R_{44} = R_{55} = \frac{d_{HH}^{ext}}{4} + \frac{d_{HH}^{IM}}{4} + \frac{d_{HC}}{5}\\
&R_{33} = R_{66} = \frac{d_{HH}^{ext}}{10} + \frac{d_{HH}^{IM}}{10}\\
&R_{77} = R_{88} = R_{99} = R_{1010} = \frac{7d_{HH}^{ext}}{20} + \frac{d_{HH}^{IM}}{4} + \frac{d_{HC}}{5}\\
&R_{79} = R_{97} = R_{810} = R_{108} = \frac{d_{HH}^{IM}}{5}\\
&R_{1111} = R_{1414} = \frac{d_{HH}^{ext}}{2} + \frac{2d_{HC}}{5}\\
&R_{1212} = R_{1313} = \frac{d_{HH}^{ext}}{2} + \frac{d_{HH}^{IM}}{10} + \frac{2d_{HC}}{5}\\
&R_{1213} = R_{1312} = -\frac{d_{HH}^{IM}}{10}\\
&R_{1515} = \frac{d_{HH}^{ext}}{5}\\
&d_{HH}^{ext} = \left(\frac{\mu_0}{4\pi}\right)^2 \frac{\hbar^2\gamma_H^4\tau_c}{r_{HH,ext}^6}\\
&d_{HH}^{IM} = \left(\frac{\mu_0}{4\pi}\right)^2 \frac{\hbar^2\gamma_H^4\tau_c}{r_{HH,IM}^6}\\
&d_{HC} = \left(\frac{\mu_0}{4\pi}\right)^2 \frac{\hbar^2\gamma_H^2\gamma_C^2\tau_c}{r_{HC}^6}
\end{aligned}
\tag{12}
$$

and the transverse and longitudinal cross-relaxation rates, σ_{ROE} and σ_{NOE}, are defined as

$$
\begin{aligned}
\sigma_{ROE} &= \frac{1}{5}\left(\frac{\mu_0}{4\pi}\right)^2 \frac{\hbar^2\gamma_H^4\tau_c}{r_{HH,IM}^6}\\
\sigma_{NOE} &= -\frac{1}{10}\left(\frac{\mu_0}{4\pi}\right)^2 \frac{\hbar^2\gamma_H^4\tau_c}{r_{HH,IM}^6}
\end{aligned}
\tag{13}
$$

where μ_0 denotes the vacuum permeability, γ_H and γ_C are the gyromagnetic ratios of ^{1}H and ^{13}C spins, respectively, $\hbar$ is Planck's constant devided by 2π, and τ_C is the correlation time (Abragam 1961; Cavanagh et al. 2007). Relaxation of longitudinal magnetization to its thermal equilibrium is not included in the calculation, as the evolution of anti-phase magnetization is considered (see below).

In our experimental scheme (Fig. 1A.1) antiphase ^{1}H$^\alpha$ magnetization ($2I_x^\alpha C_z^\alpha$) is spin-locked along its effective field using a previously described alignment element (Hansen and Kay 2007). Thus, in our simulations the initial value of the density matrix is given by

$$
\sigma(0) = \sin\theta_I 2I_x C_z + \cos\theta_I 2I_z C_z = 2I_z' C_z \tag{14}
$$

where I_z' is the aligned magnetization in the tilted frame and θ_I is the angle between the z-axis of the tilted frame and the axis parallel to the static magnetic field ($\tan\theta = \omega_1/\Omega_I$). The expectation value of the spin-locked magnetization at time T_{relax} ($M(T_{relax})$) was obtained by solving Eq. (8) and then extracting the $2I_z'C_z$ element as,

$$
M\left(T_{relax}\right) = \frac{\langle 2I_z'C_z|\sigma(T_{relax})\rangle}{\langle 2I_z'C_z|2I_z'C_z\rangle} \tag{15}
$$

In our simulations a value of $\tau_C = 2\times10^{-9}$ s was assumed, consistent with previous relaxation measurements (Kim et al. 2021), so that the corresponding cross-relaxation rates are $\sigma_{ROE} = 4.84\ s^{-1}$ and $\sigma_{NOE} = -2.42\ s^{-1}$. In all simulations, the chemical shift of spin I and the carrier position were fixed to 4.4 and 4.35 ppm, respectively ($\Omega_I = (4.4 - 4.35)\times600\times2\pi$ rad/sec), and the chemical shift of spin M was varied from 2 to 4 ppm ($\Omega_M = (2\text{ to }4 - 4.35)\times600\times2\pi$ rad/sec). The trajectory of $2I_z'C_z$ was calculated from 0 to 120 ms (fourfold longer than experimental relaxation times, Fig. 3A) with a time step of 1 ms. Similar simulations were performed in the absence of cross-relaxation by setting σ_{ROE} and σ_{NOE} to 0 in the relaxation matrix of Eq. (11).

Results and discussion

Description of pulse scheme for the measurement of ^{1}H$^\alpha$ transverse relaxation rates in IDPs

The original experiments to quantify near surface electrostatic potentials of proteins, developed by Iwahara and coworkers (Yu et al. 2021), based in part on work from the Clore group (Okuno et al. 2020), focused on the measurement of amide ^{1}H^N transverse relaxation rates in the presence and absence of variously charged spin labels. The measurement of ^{1}H^N as opposed to other proton relaxation rates has the obvious advantage in that there is only a single homonuclear scalar coupling to consider, involving ^{1}H$^\alpha$ spins, and evolution from the $^3J_{HN\text{-}H\alpha}$ coupling can be refocused by the application of a ^{1}H^N-selective 180° pulse in the center of the ^{1}H evolution period that is required to quantify transverse relaxation (Donaldson et al. 2001). Unfortunately, however, studies of IDPs at physiological pH values cannot be performed using amide correlation spectra as the rapid exchange of amide protons with water deteriorates the quality of the resulting spectra. Moreover, in such cases the relaxation of ^{1}H^N spins is contaminated by exchange with water, with effective rates that are often non-exponential. These rates, further, can vary significantly depending on where in the pulse scheme they are interrogated (Ishima et al. 1998; Yuwen et al. 2016). By contrast, relaxation rates of ^{1}H$^\alpha$ protons are not sensitive to pH (exchange with water) and ^{1}H$^\alpha$-detect experiments remain of high quality even when amide protons exchange rapidly with solvent. As the resolution of ^{1}H$^\alpha$-^{13}C$^\alpha$ correlations in 2D heteronuclear spectra of IDPs is poor, we prefer to measure relaxation data using 3D haCONHA-type experiments in which correlations of the form (ω_{CO}, ω_N, $\omega_{H\alpha}$) are recorded, exploiting the resolution in ^{13}CO and ^{15}N dimensions (Mäntylahti et al. 2011; Wong et al. 2020a). A pseudo-4D dataset is, thus, obtained, in which each 3D spectrum corresponds to a single time point that is used to quantify transverse relaxation.

Figure 1 highlights the pulse scheme that we prefer (Scheme A.1), along with a sequence that is used to cross-validate the results (Scheme A.2). For completeness, we

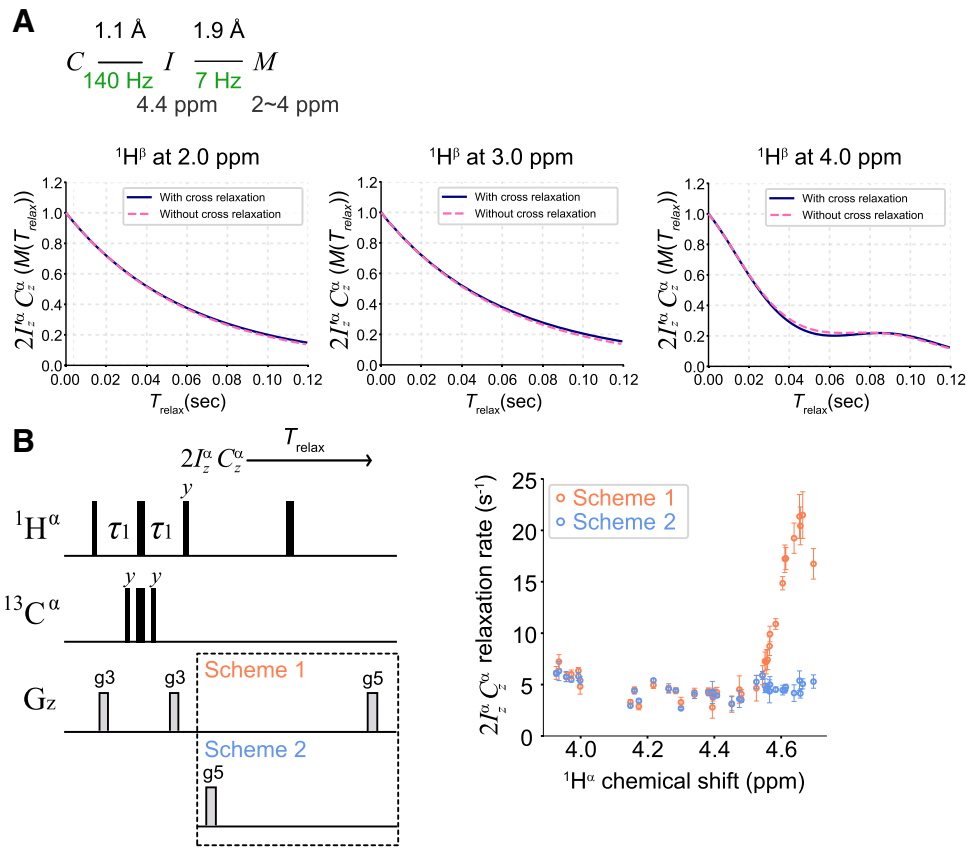

Fig. 3 Cross-relaxation has a minimal effect on the evolution of $2I'^{\alpha}_{z}C^{\alpha}_{z}$ magnetization. **A** (top) Schematic of the 3-spin {*I*, *C*, *M*}-spin system used in the simulations; a pair of external protons are included, in addition, contributing only to the auto-relaxation of proton spins *I* and *M*. (bottom) The evolution of anti-phase $^{1}H^{\alpha}$ magnetization ($2I'^{\alpha}_{z}C^{\alpha}_{z}$) spin-locked along its effective field (Eq. (14)) in the presence (navy, line) and absence (pink, dotted line) of cross-relaxation. The chemical shift of spin *M* ($^{1}H^{\beta}$ mimic) was set to 2 (left), 3 (center), and 4 (right) ppm, respectively. A 1 kHz spin-lock field is applied, centered at 4.35 ppm. Note that the distinctly non-exponential profile for the case where the $^{1}H^{\beta}$ resonance frequency is 4 ppm is due to homonuclear *J*-evolution that is not suppressed using the ^{1}H spin-lock field. **B** Relaxation of longitudinal order ($2I^{\alpha}_{z}C^{\alpha}_{z}$) was quantified using the scheme (left) that replaces A in Fig. 1. The delay τ_1 and gradient strengths of g3 and g5 are indicated in the Fig. 1 legend. Water magnetization is either initially in the transverse plane (Scheme 1) or dephased at the start of the relaxation interval (Scheme 2) during T_{relax}. The relaxation rates of $2I^{\alpha}_{z}C^{\alpha}_{z}$ two-spin order (CAPRIN1, 25 °C, 600 MHz) are shown as a function of $^{1}H^{\alpha}$ chemical shift (right)

also show a simple spin-echo variant, similar to a recently described experiment by Yu et al. (2022), to illustrate some of the challenges with recording $^{1}H^{\alpha}$ relaxation rates that must be overcome in the design of a robust pulse scheme. The initial element of the pulse sequence (A, in Fig. 1) is of interest to the relaxation experiment described here and in what follows we provide a brief overview of the magnetization pathway during this interval. Focusing on A.1, after the creation of longitudinal order ($2I^{\alpha}_{z}C^{\alpha}_{z}$) by the first INEPT element, where I^{j} and C^{j} are the proton and carbon spins that are one-bond coupled and $j = \alpha$ denotes either the $^{1}H^{\alpha}$ or $^{13}C^{\alpha}$ spin, the water magnetization is dephased by application of a pulsed field gradient to minimize the radiation damping field (gradient g4); failure to do so can lead to apparent $^{1}H^{\alpha}$ PREs that are significantly elevated, by 1.5 to 2-fold, in applications involving CAPRIN1 (see below). Subsequently, the $^{1}H^{\alpha}$ spins are locked along their respective effective fields in a manner that is efficiently achieved for the narrow $^{1}H^{\alpha}$ chemical shift range for IDPs (~4–4.8 ppm for CAPRIN1) using a 1 kHz ^{1}H continuous-wave (cw) field applied in the center of the $^{1}H^{\alpha}$ spectrum (along the *x*-axis; a ^{1}H 180_y pulse is included in the center of the cw element), and the magnetization subsequently restored to the *z*-axis prior to magnetization transfers to $^{13}CO(t_1)$ and $^{15}N(t_2)$ that are identical to those in a regular haCONHA experiment (Wong et al. 2020a).

Although the haCONHA approach circumvents issues with hydrogen exchange, other problems are introduced when using aliphatic proton spins, such as $^{1}H^{\alpha}$, and Scheme A.1 of Fig. 1 is our best attempt to minimize these. For example, $^{1}H^{\alpha}$ protons are three-bond scalar coupled to $^{1}H^{N}$ and $^{1}H^{\beta}$ spins and evolution of $^{1}H^{\alpha}$ transverse magnetization from $^{3}J_{H\alpha\text{-}H\beta}$ couplings is not as readily refocused as for $^{3}J_{HN\text{-}H\alpha}$ couplings in the context of $^{1}H^{N}$-based

measurements, for example. In a simple spin-echo scheme that might be considered for measurement of transverse relaxation rates (Fig. 1, Scheme A.3, starting from $I^{\alpha}_{x/y}$) this evolution would proceed for the complete T_{relax} period, modulating the signal, and complicating extraction of accurate transverse relaxation rates. To illustrate this, as well as our solution to the problem (Scheme A.1, starting from $2I^{\alpha}_{x}C^{\alpha}_{z}$), in more detail, we consider the "generic" spin system shown in Fig. 2A, top left, and simulate the evolution of transverse $^{1}H^{\alpha}$ x-magnetization during the spin-echo element shown in Fig. 2A, top right. We consider the case where $^{1}H^{\alpha}$ spins are locked along their respective effective fields or when the spin lock field is removed. In the simulations shown in Fig. 2A (bottom) $\omega_{H\alpha} = 4.4$ ppm and $\omega_{H\beta}$ is varied from 2 to 3.5 ppm with the orange (navy) profiles obtained with (without) the 1 kHz spin-lock field centered at 4.35 ppm. Notably, for $\omega_{H\beta} = 2$ ppm (bottom left) or 3.0 ppm (bottom center) the orange profiles are flat, as if the scalar couplings involving $^{1}H^{\alpha}$ were "turned off" ($^{3}J_{H\alpha,NH} = 7$, $^{3}J_{H\alpha,H\beta1} = 5.5$, and $^{3}J_{H\alpha,H\beta2} = 7.5$ Hz are used in the simulation). In contrast, if the spin-lock field is omitted the navy curves result, clearly showing modulation from $^{1}H^{\alpha}$–$^{1}H^{\beta}$ and $^{1}H^{\alpha}$–$^{1}H^{HN}$ scalar couplings. When the chemical shifts of the $^{1}H^{\beta}$ protons are increased to 3.5 ppm (bottom right), closer to the position of the spin lock, a slight amount of modulation (approximately 1–2%—between 1 and 0.98) is obtained for the spin lock case.

It is noteworthy that in IDPs all $^{1}H^{\beta}$ protons resonate upfield of 3.5 ppm with the exception of those from Ser and Thr (Wishart et al. 1995), so that flat profiles (*i.e.*, unmodulated by homonuclear scalar couplings) would be expected for all non-Ser/Thr $^{1}H^{\alpha}$ protons using a spin lock scheme to measure relaxation. As might be expected, the presence of more spins on the side-chain does not affect the trajectory of x-magnetization, as shown in the simulation for a Met spin system containing 6 spins, where random coil chemical shifts are taken from Wishart et al. (1995) (Fig. 2B, left). The proximity of $^{1}H^{\alpha}$ and $^{1}H^{\beta}$ chemical shifts in Ser ($\omega_{H\alpha} = 4.47$ ppm, $\omega_{H\beta} = \{3.87, 3.89\}$ ppm) leads to significant modulation that cannot be suppressed by the ^{1}H spin-lock field (Fig. 2B, center), with a similar situation occurring for Thr (Fig. 2B, right). For both of these residues homonuclear J-modulation simply decreases magnetization intensity; there is no net transfer of observable magnetization between spins, as there would be in a Hartmann-Hahn scheme where in-phase $^{1}H^{\alpha/\beta\cdots}$ magnetization is initially created. This is because the initial magnetization for each proton is anti-phase with respect to its attached carbon and ^{13}C–^{1}H scalar coupled evolution is largely suppressed by the ^{1}H cw field. Thus, while the transfer, $2I^{\alpha}_{x}C^{\alpha}_{z} \overset{J_{H\alpha H\beta}}{\rightarrow} 2I^{\beta}_{x}C^{\alpha}_{z}$, does occur, the transfer, $2I^{\beta}_{x}C^{\beta}_{z} \overset{J_{H\alpha H\beta}}{\rightarrow} 2I^{\alpha}_{x}C^{\alpha}_{z}$, does not, with only antiphase magnetization of the form $2I^{\alpha}_{x}C^{\alpha}_{z}$ ultimately detected. This ensures that the measured $^{1}H^{\alpha}$ relaxation rates are not 'contaminated' by contributions from relaxation of other scalar coupled protons in the case of Ser and Thr. For $^{1}H^{\alpha}$ spins from these residues, however, the scalar coupled evolution, $2I^{\alpha}_{x}C^{\alpha}_{z} \overset{J_{H\alpha H\beta}}{\rightarrow} 2I^{\beta}_{x}C^{\alpha}_{z}$, prohibits extraction of accurate relaxation rates from exponential fits of the "decay" curves. In contrast, as J-coupled modulation of non-Ser/Thr $^{1}H^{\alpha}$ protons does not occur, there is no "leakage" of magnetization from $2I^{\alpha}_{x}C^{\alpha}_{z}$ to $2I^{\beta}_{x}C^{\alpha}_{z}$ in these cases, and exponential decays are expected. Finally, for Gly, the $^{1}H^{\alpha}$ spins become very strongly coupled in the presence of the cw field (*i.e.*, essentially equivalent), and the sum of $^{1}H^{\alpha}$ magnetization does not evolve under scalar coupling in this limiting case since $\left[I^{\alpha 1}_{x} + I^{\alpha 2}_{x}, \boldsymbol{I}^{\alpha 1} \cdot \boldsymbol{I}^{\alpha 2}\right] = 0$, where [] denotes the commutator operation. Thus, flat profiles are observed for the $^{1}H^{\alpha}$ spins of Gly in simulations even when scalar coupled evolution is considered. Of course, even in the case where the two $^{1}H^{\alpha}$ Gly spins are resolved (typically with chemical shift differences of 0.05–0.1 ppm), the observed relaxation rates would represent the average of the values from the two H^{α} positions, which are expected to be very similar, as magnetization is very efficiently transferred between the $^{1}H^{\alpha}$ spins during the application of the spin-lock. It is worth noting that complications from J-modulation can be prevalent in non-^{1}H homonuclear spin systems and similar strategies involving band-selective locking schemes have been used previously to measure $^{13}C^{\alpha}$ relaxation rates in uniformly ^{13}C-labeled proteins (Yamazaki et al. 1994).

Figure 2 illustrates the importance of the ^{1}H cw spin-lock field in the suppression of homonuclear J-modulation of magnetization for the majority of the spin systems in IDPs. Spin-locking of magnetization can, however, potentially lead to non-exponential relaxation from magnetization transfer mediated by dipolar cross-relaxation (spin diffusion). As described above, in the context of magnetization transfer through scalar couplings, the dipolar transfer can also be minimized by recording relaxation rates of $^{1}H^{\alpha}$ magnetization that is anti-phase with respect to the one-bond coupled ^{13}C (Sekhar et al. 2016). Thus, in the case of a pair of dipolar coupled ^{1}H spins, I and M, relaxation proceeds as

$$\frac{d2I'_{z}C^{I}_{z}}{dt} = -\rho_{I'}2I'_{z}C^{I}_{z} - \sigma_{I'M'}2M'_{z}C^{I}_{z} \tag{16}$$

where $\rho_{I'}$ and $\sigma_{I'M'}$ are auto- and cross-relaxation rates of the aligned magnetization in the tilted spin-lock frame that is germane for spin-locked magnetization considered in our experiments (the primes in I'_{z} and M'_{z} denote 'tilted' magnetization). As hetero-spins M and C^{I} are not scalar coupled (C^{I} is one bond coupled to proton spin I) there is no longitudinal order of the form $2M'_{z}C^{I}_{z}$ initially so that the decay of the magnetization of interest is essentially single exponential,

with magnetization transfer between $2M'_zC^I_z$ and $2I'_zC^I_z$ effectively suppressed over the relatively short range of relaxation times considered ($T_{\text{relax\_max}} = 30$ ms in our experiments). This is in contrast to what would be expected if the relaxation of in-phase ^{1}H magnetization was quantified. Figure 3A illustrates the evolution of anti-phase I spin magnetization during the relaxation element for a 3-spin {I, C, M}-spin system, with the chemical shift of the M spin varied between 2 and 4 ppm; cross-relaxation introduces a negligible effect, using an effective I–M distance of 1.9 Å for relaxation times extending to 120 ms and for a rotational correlation time of 2 ns, appropriate for the experimental system considered here (Kim et al. 2021). Note that the evolution of magnetization is decidedly non-exponential when $\omega_{H\beta} = 4$ ppm, due to I–M scalar coupled evolution.

The importance of "water" management, even in ^{1}H$^\alpha$-based experiments is illustrated in Fig. 3B. Here, by means of example, we consider the relaxation of longitudinal order, $2I^\alpha_zC^\alpha_z$, during an interval, T_{relax}, where a gradient that dephases water is applied either at the start or the end of the relaxation period. If the water transverse magnetization is not dephased initially, its precession induces an oscillating current in the receiver coil, and hence, a magnetic field, oscillating at the frequency of precession. This induced field rotates water magnetization and other spins resonating close to the water line back to their equilibrium (Krishnan and Murali 2013). Thus, the effect of the induced magnetic field would be expected to be more pronounced for ^{1}H$^\alpha$ spins whose chemical shifts are closer to the water line. With this in mind, the measured longitudinal order relaxation rate for each ^{1}H$^\alpha$–^{13}C$^\alpha$ spin pair in CAPRIN1 (described below) is plotted as a function of ^{1}H$^\alpha$ chemical shift, showing a clear elevation in rates for spins resonating near the water line when water is not dephased. As the water is initially in the transverse plane in this experiment, as it would be at point a in Schemes A.1–A.3 of Fig. 1 the radiation-damping field from bulk water can be considerable, unless water magnetization is initially dephased (Saturation of the water line significantly attenuates sensitivity of the experiment and is not a good option). Similar experiments, starting from anti-phase ^{1}H$^\alpha$ magnetization ($2I^\alpha_xC^\alpha_z$), show a 1.5- to 2-fold increase in measured ^{1}H$^\alpha$ PRE rates, in the absence of dephasing. Water magnetization is therefore dephased in schemes A.1 and A.2 immediately after the initial INEPT transfer and prior to the T_{relax} period.

Experimental validation

The RNA binding protein CAPRIN1 has been shown to play an essential role in the formation of neuronal and stress granules in cells (Kedersha et al. 2016; Nakayama et al. 2017), and the C-terminal low complexity disordered region comprising residues 607–709, and referred to in what follows as CAPRIN1, phase separates in vitro (Kim et al. 2019). Because of the small size of CAPRIN1 it has been used as a model system in our laboratory, both for the development of NMR methodology for characterizing IDPs in condensates, and, importantly, to understand the interactions that give rise to phase separation in the first place (Kim et al. 2021). CAPRIN1 has a pI of 11.5 and a charge of + 13 under the conditions of our experiments and the resulting unfavorable electrostatic interactions between proximal molecules must be screened before phase separation can occur. This can be achieved typically by the addition of negatively charged molecules or by adding salt (Kim et al. 2019; Wong et al. 2020a). Here we have used low salt buffers (25 mM MES-NaOH (pH 5.5) or 25 mM HEPES–NaOH (pH 7.4)) to ensure that the protein solutions studied are fully mixed (*i.e.*, not phase separated), and, therefore, CAPRIN1 is expected to have a positive electrostatic potential, as established below. Figure 4A, top, shows the ^{13}CO–^{15}N projection of a 3D haCONHA dataset recorded with the pulse sequence of Fig. 1 (Scheme A.1), $T_{relax} = 0$ ms, along with the magnetization transfer pathway that gives rise to the spectrum (bottom). Three peaks are highlighted, along with the residues from where the correlations originate; analysis of these peaks in a series of 3D datasets recorded as a function of T_{relax}, generates the decay curves in Fig. 4B. As our goal is to calculate the near surface electrostatic potential (Yu et al. 2021) of CAPRIN1, we have measured ^{1}H$^\alpha$ transverse relaxation rates in the presence or absence (Diamagnetic, purple) of 5 mM negative (Carboxy-PROXYL, red) or neutral (Carbamoyl-PROXYL, grey) solvent spin labels. A comparison of intensity profiles using Schemes A.3 and A.1 (titled Scheme A.3 and Scheme A.1 in the figure) clearly shows the effects of scalar coupling on the evolution of ^{1}H$^\alpha$ magnetization when recording data with the spin-echo scheme (Fig. 1A.3) relative to the spin-lock element of Fig. 1A.1. Notably, J-modulation gives rise to decidedly non-exponential decays of ^{1}H$^\alpha$ magnetization (left column, Scheme A.3), as is particularly apparent in the profile of G609, where the magnetization becomes negative for T_{relax} values in excess of approximately 20 ms. The effective intensity decays are slower when using the spin-lock, including for T705, despite the fact that scalar coupling effects are not completely eliminated for ^{1}H$^\alpha$ spins of this residue when magnetization is locked (see above).

Recognizing the deleterious effects of homonuclear scalar couplings to the measurement of ^{1}H$^\alpha$ relaxation rates using spin-echo type experiments (Fig. 1A.3), Iwahara and co-workers determined PRE rates by simultaneous analysis of the ratios of signal intensities in paramagnetic and diamagnetic samples in spectra recorded with identical T_{relax} values (Iwahara et al. 2004; Clore and Iwahara 2009; Yu et al. 2022). In this way the scalar coupling terms cancel,

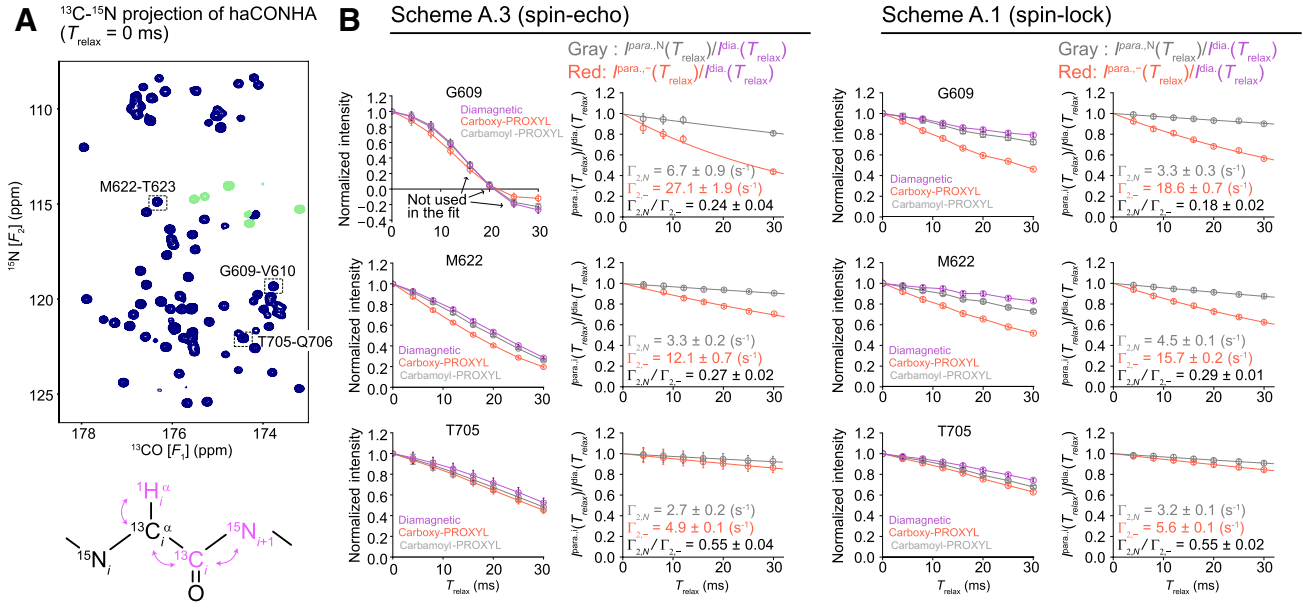

Fig. 4 Suppression of *J*-modulation via spin locking of $^{1}H^{\alpha}$ magnetization. **A** ^{13}CO-^{15}N projection of a 3D haCONHA dataset recorded with the pulse sequence of Fig. 1A.1, T_{relax} = 0 ms. Several peaks are highlighted from which the $^{1}H^{\alpha}$ relaxation profiles shown are derived. The magnetization transfer pathway is indicated at the bottom. **B** Decay curves of selected residues measured in the presence or absence (Diamagnetic, purple) of 5 mM negative (carboxy-PROXYL, red) or neutral (carbamoyl-PROXYL, grey) solvent spin labels. Solid lines connect the experimental points in the panels titled Scheme A.3 and Scheme A.1. Ratio of corresponding peak intensities in spectra recorded with the sequences of either Fig. 1A.3 (left) or Fig. 1A.1 (right) and either with, $I^{para.i}(T_{relax})$, or without, $I^{dia.}(T_{relax})$, solvent spin-labels, along with exponential fits of the data and extracted PRE rates, are shown. All measurements were performed on a 300 µM U-^{13}C, ^{15}N CAPRIN1 sample at pH 5.5, 25 °C and 14.0 Tesla

and ratios are sensitive only to the PRE. However, the signal intensities themselves are reduced by the modulation making this approach more error prone than if coupled evolution was not present in the first place. For example, the large germinal $^{1}H^{\alpha}$ coupling in Gly residues results in low peak intensities for T_{relax} values greater than approximately 15 ms (Fig. 4B); in our applications T_{relax} values between 16 and 25 ms had to be omitted when data were recorded using a spin-echo based sequence (Fig. 1A.3). For other residue-types (non-Gly residues), the reduction in intensities of resonances is less severe, on average a ratio of 0.46 ± 0.12 for T_{relax} = 30 ms is obtained, when comparing the schemes shown in Fig. 1A.1 and A.3. Also shown in Fig. 4B are exponential fits of intensity ratios, $I^{para.,i}(T_{relax})/I^{dia.}(T_{relax})$, of cross-peaks from spectra recorded with the spin-echo and spin-lock schemes. Notably, while the PRE rates from Schemes A.1 and A.3 are somewhat different, the ratio of rates recorded with different combinations of solvent spin labels tends to be similar (with the exception of a number of Gly residues, for which the germinal coupling is particularly detrimental for the spin-echo scheme).

The simulations and experimental data presented in Figs. 2, 3, and 4 strongly suggest that the spin-lock scheme of Fig. 1A.1 suppresses *J*-modulation (except for $^{1}H^{\alpha}$ from Ser and Thr) without introducing magnetization transfer via the ROE. A more rigorous evaluation of the robustness of the experiment can be made through comparison to an analogous yet distinct approach, illustrated in Fig. 1A.2 where the relaxation of transverse (not spin-locked) $^{1}H^{\alpha}$ magnetization is measured. In this pulse scheme suppression of $^{1}H^{\alpha}$-^{1}H scalar coupled evolution is achieved for the majority of amino acids through the use of band-selective ^{1}H adiabatic decoupling (Kupce and Wagner 1996) that is carefully adjusted so as to minimally perturb the $^{1}H^{\alpha}$ signals of interest, while decoupling $^{1}H^{\beta}$ and $^{1}H^{N}$ proton spins. Since adiabatic decoupling of $^{1}H^{\beta}$ is applied over a chemical shift range of ~ 2.2 ± 1.1 ppm, Ser, and Thr, whose $^{1}H^{\beta}$ chemical shifts do not fall within this region (and overlap with those of $^{1}H^{\alpha}$) are not effectively decoupled. In addition, the large germinal (two-bond) $^{1}H^{\alpha1}$–$^{1}H^{\alpha2}$ coupling (~ −15 Hz) for Gly results in a severe modulation of the $^{1}H^{\alpha}$ signals for this residue, as is observed in experiments recorded with Fig. 1A.3. Figure 5 compares carboxy-PROXYL PRE values obtained via the schemes of Fig. 1A.1 and A.2 omitting Gly residues, and the agreement is excellent (RMSD = 0.69 s^{-1} for $\Gamma_{2,-}$, significantly better than when PRE rates are compared between spin-echo (Fig. 1A.3) and spin lock (Fig. 1A.1) schemes (RMSD = 2.21 s^{-1}). Thus, accurate PRE values are obtained

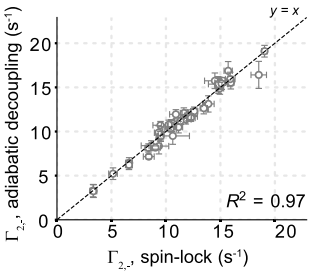

Fig. 5 Correlation plot of carboxy-PROXYL $^1H^\alpha$ PRE rates using schemes A.1 and A.2 of Fig. 1. The carboxy-PROXYL $^1H^\alpha$ PRE rates ($\Gamma_{2,-}$ =paramagnetic − diamagnetic) measured using two schemes of Fig. 1 are plotted. The PRE rates plotted along the *y*-axis were measured using a ^1H adiabatic decoupling approach (A.2) and those plotted along the *x*-axis were quantified via a spin-lock element (A.1). PRE measurements were performed on a 300 µM U-^{13}C, ^{15}N CAPRIN1 sample at pH 5.5, 25 °C and 14.0 Tesla, with and without 5 mM 3-carboxy-PROXYL. R^2 is the squared Pearson correlation coefficient

by using the ^1H cw spin-lock field in Fig. 1A.1, without deleterious effects from residual *J*-evolution or cross-relaxation. As the $^1H^\alpha$ signals from Gly residues are not modulated by geminal scalar couplings using the sequence of Fig. 1A.1, we prefer it, and in what follows all results were obtained using this experiment.

Figure 6A shows ^{15}N–$^1H^N$ TROSY-HSQC spectra of CAPRIN1 recorded at pH 5.5 (left) and at pH 7.4 (center); all other experimental conditions are identical. The degradation of spectral quality with pH is obvious. However, the ^{13}CO–^{15}N projection of the 3D haCONHA dataset (non-TROSY acquisition in the ^{15}N dimension) recorded on the pH 7.4 sample is of high quality (right), so that electrostatic potentials (ϕ_{ENS}) can be obtained at neutral pH values using relaxation rates measured with the sequence of Fig. 1A.1. A comparison of ϕ_{ENS} values measured at pH 5.5 using haCONHA and ^{15}N-$^1H^N$ TROSY pulse schemes is presented in Fig. 6B, C (left), with good agreement between the two

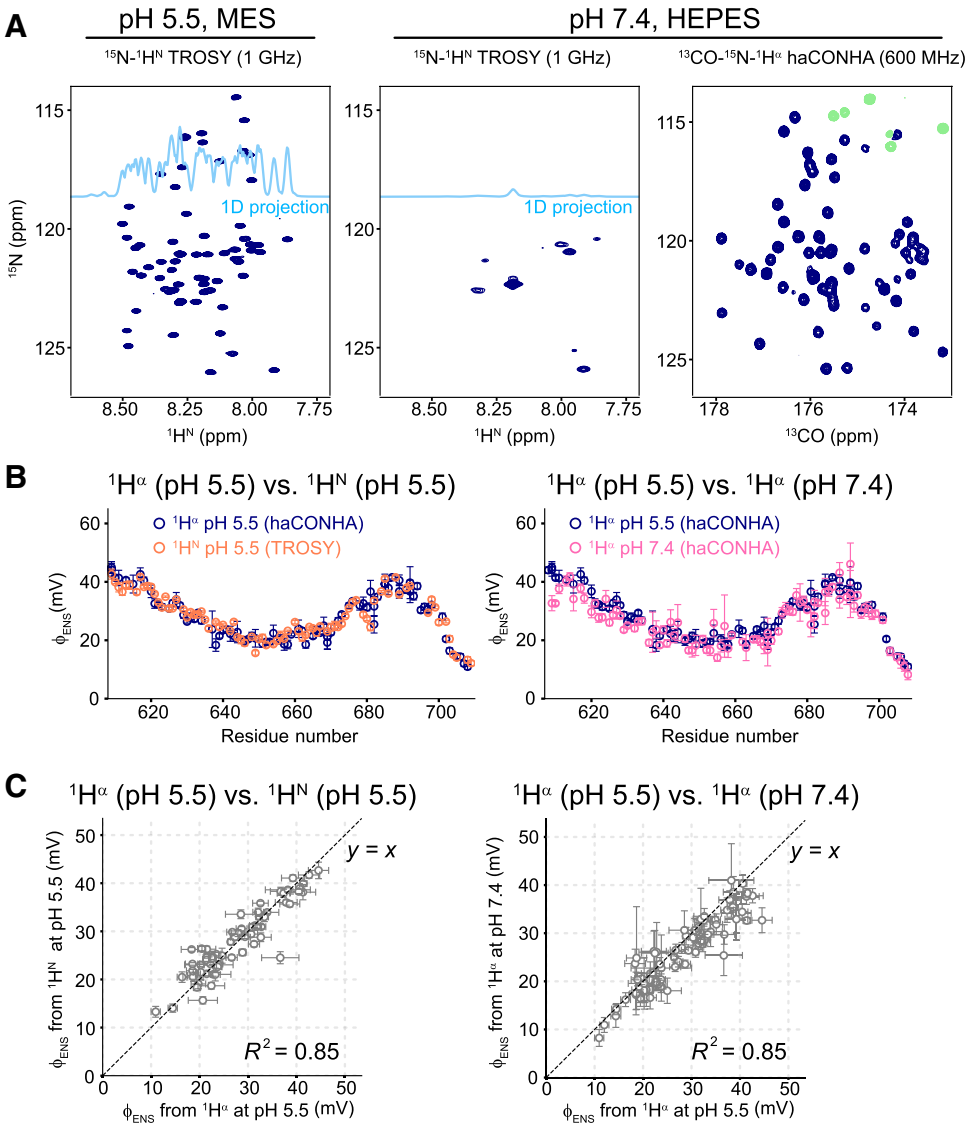

Fig. 6 Validation of the methodology. **A** ^{15}N-$^1H^N$ TROSY-HSQC spectra of CAPRIN1 recorded at pH 5.5 (left) and at pH 7.4 (center) with all other experimental conditions identical (25 °C, 23.5 T), along with a ^{13}CO-^{15}N projection of the 3D haCONHA dataset (right, pH 7.4, 14.0 T) **B**, **C** comparison of ϕ_{ENS} values measured at pH 5.5 using haCONHA and ^{15}N-$^1H^N$ TROSY pulse schemes (left) and between ϕ_{ENS} values measured at pH 5.5 and pH 7.4 using the haCONHA experiment (right)

methods. A strong correlation between ϕ_{ENS} values measured at pH 5.5 and pH 7.4 is also found (Fig. 6B, C, right), as expected, since CAPRIN1 does not contain His residues. Slightly higher errors in the haCONHA based ϕ_{ENS} measurements at pH 7.4 are noted compared to those at pH 5.5. This reflects the fact that solvent exchange is close to two orders of magnitude more rapid at the higher pH so that the amide protons are more effectively saturated through exchange with water (that is saturated using this pulse scheme). In turn, this leads to saturation transfer to the $^1H^\alpha$ protons via spin-diffusion, decreasing the initial $^1H^\alpha$ polarization and hence the resulting signal intensities in 3D datasets.

Concluding remarks

Herein we have described a robust method for the measurement of backbone $^1H^\alpha$ relaxation rates in IDPs, a first step for obtaining near surface electrostatic potentials of IDPs at neutral pH values. The experiment avoids $^1H^N$ magnetization, leading to high quality IDP spectra even when recorded at high pH where solvent exchange can often be a limiting factor. A number of issues associated with the measurement of $^1H^\alpha$ relaxation in fully protonated protein systems are discussed and solutions presented so that robust rates can be obtained. Notably, the use of a band-selective spin-lock significantly suppresses homonuclear scalar coupling modulation for all $^1H^\alpha$ protons, except those from Ser and Thr, improving the accuracy of measured PRE values, since signal decay is attenuated only by relaxation. The excellent agreement between PRE rates measured using ^1H spin-lock and ^1H adiabatic decoupling schemes, the close correlation between ϕ_{ENS} values measured on CAPRIN1 at pH 5.5 using $^1H^N$- and $^1H^\alpha$-based experiments, where amide exchange is not limiting, and the good agreement for CAPRIN1 ϕ_{ENS} calculated from experiments on samples at pH 5.5 and 7.4 (where exchange is severe), provides strong confidence in the developed methodology. During the completion of this study we became aware of related work by Yu et al (2022) where $^1H^\alpha$ transverse relaxation rates were used to establish the surface potential of ubiquitin using 2D (HCACO)NH-based experiments. This approach is most clearly appropriate for studies of folded proteins where solvent exchange is not limiting, although it seems likely that here, too, there would be considerable benefit with spin-locking of $^1H^\alpha$ magnetization during the relaxation measurement. This work sets the stage for the measurement of electrostatic potentials in CAPRIN1 condensates, in order to establish the role of electrostatics in phase separation.

Acknowledgements We thank Dr. Enrico Rennella (University of Toronto) for help with time-domain fitting of pseudo-4D datasets. Y.T. is supported through a Japan Society for the Promotion of Science Overseas Research Fellowship, an Uehara Memorial Foundation post-doctoral fellowship, and a fellowship from the Canadian Institutes of Health Research (CIHR). A.K.R is grateful to the CIHR for post-doctoral support. This research was funded through grants from the CIHR and the Natural Sciences and Engineering Research Council of Canada.

Data availability The datasets generated during and/or analyzed during the current study are available from the corresponding authors upon reasonable request.

References

Abragam A (1961) Principles of nuclear magnetism. Clarendon Press, Oxford

Allard P, Helgstrand M, Härd T (1997) A method for simulation of NOESY, ROESY, and off-resonance ROESY spectra. J Magn Reson 129:19–29. https://doi.org/10.1006/jmre.1997.1252

Allard P, Helgstrand M, Härd T (1998) The complete homogeneous master equation for a heteronuclear two-spin system in the basis of cartesian product operators. J Magn Reson 134:7–16. https://doi.org/10.1006/jmre.1998.1509

Anthis NJ, Clore GM (2015) Visualizing transient dark states by NMR spectroscopy. Q Rev Biophys 1:35–116. https://doi.org/10.1017/S0033583514000122

Cavanagh J, Fairbrother WJ, Palmer AG III et al (2007) Protein NMR spectroscopy: principles and practice, 2nd edn. Academic Press

Clore GM, Iwahara J (2009) Theory, practice, and applications of paramagnetic relaxation enhancement for the characterization of transient low-population states of biological macromolecules and their complexes. Chem Rev 109:4108–4139. https://doi.org/10.1021/cr900033p

Delaglio F, Grzesiek S, Vuister G et al (1995) NMRPipe: a multidimensional spectral processing system based on UNIX pipes. J Biomol NMR 6:277–293. https://doi.org/10.1007/BF00197809

Desvaux H, Berthault P, Birlirakis N, Goldman M (1994) Off-resonance ROESY for the study of dynamic processes. J Magn Reson Ser A 108:219–229. https://doi.org/10.1006/jmra.1994.1114

Donaldson LW, Skrynnikov NR, Choy W-Y et al (2001) Structural Characterization of proteins with an attached ATCUN motif by paramagnetic relaxation enhancement NMR spectroscopy. J Am Chem Soc 123:9843–9847. https://doi.org/10.1021/ja011241p

Ernst RR, Bodenhausen G, Wokaun A (1987) Principles of nuclear magnetic resonance in one and two dimensions. Clarendon Press, Oxford

Geen H, Freeman R (1991) Band-selective radiofrequency pulses. J Magn Reson 93:93–141. https://doi.org/10.1016/0022-2364(91)90034-Q

Goto NK, Gardner KH, Mueller GA et al (1999) A robust and cost-effective method for the production of Val, Leu, Ile (δ1) methyl-protonated ^{15}N-, ^{13}C-, ^{2}H-labeled proteins. J Biomol NMR 13:369–374. https://doi.org/10.1023/A:1008393201236

Grzesiek S, Anglister J, Bax A (1993) Correlation of backbone amide and aliphatic side-chain resonances in $^{13}C/^{15}N$-enriched proteins by isotropic mixing of ^{13}C magnetization. J Magn Reson Ser B 101:114–119. https://doi.org/10.1006/jmrb.1993.1019

Hähnke MJ, Richter C, Heinicke F, Schwalbe H (2010) The HN(COCA)HAHB NMR experiment for the stereospecific assignment of H_β-protons in non-native states of proteins. J Am Chem Soc 132:918–919. https://doi.org/10.1021/ja909239w

Hansen DF, Kay LE (2007) Improved magnetization alignment schemes for spin-lock relaxation experiments. J Biomol NMR 37:245–255. https://doi.org/10.1007/s10858-006-9126-6

Hansen AL, Lundström P, Velyvis A, Kay LE (2012) Quantifying millisecond exchange dynamics in proteins by CPMG relaxation dispersion NMR using side-chain ^{1}H probes. J Am Chem Soc 134:3178–3189. https://doi.org/10.1021/ja210711v

Helmus JJ, Jaroniec CP (2013) Nmrglue: an open source Python package for the analysis of multidimensional NMR data. J Biomol NMR 55:355–367. https://doi.org/10.1007/s10858-013-9718-x

Hyberts SG, Takeuchi K, Wagner G (2010) Poisson-gap sampling and forward maximum entropy reconstruction for enhancing the resolution and sensitivity of protein NMR data. J Am Chem Soc 132:2145–2147. https://doi.org/10.1021/ja908004w

Ishima R, Wingfield PT, Stahl SJ et al (1998) Using amide ^{1}H and ^{15}N transverse relaxation to detect millisecond time-scale motions in perdeuterated proteins: application to HIV-1 protease. J Am Chem Soc 120:10534–10542. https://doi.org/10.1021/ja981546c

Ishima R, Louis JM, Torchia DA (1999) Transverse ^{13}C relaxation of CHD_2 methyl isotopmers to detect slow Conformational changes of protein side chains. J Am Chem Soc 121:11589–11590. https://doi.org/10.1021/ja992836b

Iwahara J, Schwieters CD, Clore GM (2004) Ensemble approach for NMR structure refinement against ^{1}H paramagnetic relaxation enhancement data arising from a flexible paramagnetic group attached to a macromolecule. J Am Chem Soc 126:5879–5896. https://doi.org/10.1021/ja031580d

Iwahara J, Tang C, Marius Clore G (2007) Practical aspects of ^{1}H transverse paramagnetic relaxation enhancement measurements on macromolecules. J Magn Reson 184:185–195. https://doi.org/10.1016/j.jmr.2006.10.003

Kainosho M, Torizawa T, Iwashita Y et al (2006) Optimal isotope labelling for NMR protein structure determinations. Nature 440:52–57. https://doi.org/10.1038/nature04525

Kasinath V, Valentine KG, Wand AJ (2013) A ^{13}C labeling strategy reveals a range of aromatic side chain motion in calmodulin. J Am Chem Soc 135:9560–9563. https://doi.org/10.1021/ja4001129

Kay LE, Torchia DA (1991) The effects of dipolar cross correlation on ^{13}C methyl-carbon T_1, T_2, and NOE measurements in macromolecules. J Magn Reson 95:536–547. https://doi.org/10.1016/0022-2364(91)90167-R

Kay LE, Torchia DA, Bax A (1989) Backbone dynamics of proteins AS studied by 15N inverse detected heteranuckar. Biochemistry 28:8972–8979

Kay LE, Ikura M, Tschudin R, Bax A (1990) Three-dimensional triple-resonance NMR spectroscopy of isotopically enriched proteins. J Magn Reson 89:496–514. https://doi.org/10.1016/0022-2364(90)90333-5

Kay LE, Muhandiram DR, Wolf G et al (1998) Correlation between binding and dynamics at SH2 domain interfaces. Nat Struct Biol 5:156–163. https://doi.org/10.1038/nsb0298-156

Kedersha N, Panas MD, Achorn CA et al (2016) G3BP–Caprin1–USP10 complexes mediate stress granule condensation and associate with 40S subunits. J Cell Biol. https://doi.org/10.1083/jcb.201508028

Kim TH, Tsang B, Vernon RM et al (2019) Phospho-dependent phase separation of FMRP and CAPRIN1 recapitulates regulation of translation and deadenylation. Science 365:825–829. https://doi.org/10.1126/science.aax4240

Kim TH, Payliss BJ, Nosella ML et al (2021) Interaction hot spots for phase separation revealed by NMR studies of a CAPRIN1 condensed phase. Proc Natl Acad Sci 118:e2104897118. https://doi.org/10.1073/pnas.2104897118

Krishnan VV, Murali N (2013) Radiation damping in modern NMR experiments: progress and challenges. Prog Nucl Magn Reson Spectrosc 68:41–57. https://doi.org/10.1016/j.pnmrs.2012.06.001

Kupce E, Freeman R (1995) Adiabatic pulses for wideband inversion and broadband decoupling. J Magn Reson Ser A 115:273–276

Kupce E, Wagner G (1996) Multisite band-selective decoupling in proteins. J Magn Reson 110:309–312. https://doi.org/10.1006/jmrb.1996.0048

Lipari G, Szabo A (1982a) Model-free approach to the interpretation of nuclear magnetic resonance relaxation in macromolecules. 1. Theory and range of validity. J Am Chem Soc 104:4546–4559. https://doi.org/10.1021/ja00381a009

Lipari G, Szabo A (1982b) Model-free approach to the interpretation of nuclear magnetic resonance relaxation in macromolecules. 2. Analysis of experimental results. J Am Chem Soc 104:4559–4570. https://doi.org/10.1021/ja00381a010

Logan TM, Olejniczak ET, Xu RX, Fesik SW (1993) A general method for assigning NMR spectra of denatured proteins using 3D HC(CO)NH-TOCSY triple resonance experiments. J Biomol NMR 3:225–231. https://doi.org/10.1007/BF00178264

Long D, Delaglio F, Sekhar A, Kay LE (2015) Probing invisible, excited protein states by non-uniformly sampled pseudo-4D CEST spectroscopy. Angew Chemie Int Ed 54:10507–10511. https://doi.org/10.1002/anie.201504070

Lundström P, Teilum K, Carstensen T et al (2007) Fractional ^{13}C enrichment of isolated carbons using [1-^{13}C]- or [2-^{13}C]-glucose facilitates the accurate measurement of dynamics at backbone C^{α} and side-chain methyl positions in proteins. J Biomol NMR 38:199–212. https://doi.org/10.1007/s10858-007-9158-6

Lundström P, Hansen DF, Vallurupalli P, Kay LE (2009) Accurate measurement of alpha proton chemical shifts of excited protein states by relaxation dispersion NMR spectroscopy. J Am Chem Soc 131:1915–1926. https://doi.org/10.1021/ja807796a

Mäntylahti S, Hellman M, Permi P (2011) Extension of the HA-detection based approach: (HCA)CON(CA)H and (HCA)NCO(CA)H experiments for the main-chain assignment of intrinsically disordered proteins. J Biomol NMR 49:99–109. https://doi.org/10.1007/s10858-011-9470-z

Marion D, Ikura M, Tschudin R, Bax A (1989) Rapid recording of 2D NMR spectra without phase cycling. Application to the study of hydrogen exchange in proteins. J Magn Reson 85:393–399. https://doi.org/10.1016/0022-2364(89)90152-2

Millet O, Muhandiram DR, Skrynnikov NR, Kay LE (2002) Deuterium spin probes of side-chain dynamics in proteins. 1. Measurement of five relaxation rates per deuteron in ^{13} C-labeled and fractionally ^{2}H-enriched proteins in solution. J Am Chem Soc 124:6439–6448. https://doi.org/10.1021/ja012497y

Mittermaier A, Kay LE (2006) New tools provide new insights in NMR studies of protein dynamics. Science 312:224–228. https://doi.org/10.1126/science.1124964

Muhandiram DR, Yamazaki T, Sykes BD, Kay LE (1995) Measurement of ^{2}H T_1 and $T_{1\rho}$. relaxation times in uniformly ^{13}C-labeled and fractionally ^{2}H-labeled proteins in solution. J Am Chem Soc 117:11536–11544. https://doi.org/10.1021/ja00151a018

Nakayama K, Ohashi R, Shinoda Y et al (2017) RNG105/caprin1, an RNA granule protein for dendritic mRNA localization, is essential for long-term memory formation. Elife. https://doi.org/10.7554/eLife.29677

Okuno Y, Szabo A, Clore GM (2020) Quantitative interpretation of solvent paramagnetic relaxation for probing protein-cosolute interactions. J Am Chem Soc 142:8281–8290. https://doi.org/10.1021/jacs.0c00747

Palmer AG (2014) Chemical exchange in biomacromolecules: past, present, and future. J Magn Reson 241:3–17. https://doi.org/10.1016/j.jmr.2014.01.008

Pervushin K, Riek R, Wider G, Wüthrich K (1997) Attenuated T_2 relaxation by mutual cancellation of dipole-dipole coupling and chemical shift anisotropy indicates an avenue to NMR structures of very large biological macromolecules in solution. Proc Natl Acad Sci USA 94:12366–12371. https://doi.org/10.1073/pnas.94.23.12366

Sekhar A, Rosenzweig R, Bouvignies G, Kay LE (2016) Hsp70 biases the folding pathways of client proteins. Proc Natl Acad Sci USA. https://doi.org/10.1073/pnas.1601846113

Sørensen OW, Eich GW, Levitt MH et al (1984) Product operator formalism for the description of NMR pulse experiments. Prog Nucl Magn Reson Spectrosc 16:163–192. https://doi.org/10.1016/0079-6565(84)80005-9

Sun H, Kay LE, Tugarinov V (2011) An optimized relaxation-based coherence transfer NMR experiment for the measurement of side-chain order in methyl-protonated, highly deuterated proteins. J Phys Chem B 115:14878–14884. https://doi.org/10.1021/jp209049k

Teilum K, Brath U, Lundström P, Akke M (2006) Biosynthetic ^{13}C labeling of aromatic side chains in proteins for NMR relaxation measurements. J Am Chem Soc 128:2506–2507. https://doi.org/10.1021/ja055660o

Tugarinov V, Clore G (2021) The measurement of relaxation rates of degenerate ^{1}H transitions in methyl groups of proteins using acute angle radiofrequency pulses. J Magn Reson 330:107034. https://doi.org/10.1016/j.jmr.2021.107034

Tugarinov V, Kay LE (2005) Methyl groups as probes of structure and dynamics in NMR studies of high-molecular-weight proteins. ChemBioChem 6:1567–1577. https://doi.org/10.1002/cbic.200500110

Vallurupalli P, Bouvignies G, Kay LE (2013) A computational study of the effects of 13C–13C scalar couplings on 13C CEST NMR spectra: towards studies on a uniformly 13C-labeled protein. ChemBioChem 14:1709–1713. https://doi.org/10.1002/cbic.201300230

Vold RR, Vold RL (1976) Transverse relaxation in heteronuclear coupled spin systems: AX, AX_2, AX_3, and AXY. J Chem Phys 64:320–332. https://doi.org/10.1063/1.431924

Werbelow LG, Grant DM (1977) Intramolecular dipolar relaxation in multispin systems. In: Advances in magnetic and optical resonance, pp 189–299

Wishart DS, Bigam CG, Holm A et al (1995) ^{1}H, ^{13}C and ^{15}N random coil NMR chemical shifts of the common amino acids. I. Investigations of nearest-neighbor effects. J Biomol NMR 5:67–81. https://doi.org/10.1007/BF00227471

Wong LE, Kim TH, Muhandiram DR et al (2020a) NMR experiments for studies of dilute and condensed protein phases: application to the phase-separating protein CAPRIN1. J Am Chem Soc 142:2471–2489. https://doi.org/10.1021/jacs.9b12208

Wong LE, Kim TH, Rennella E et al (2020b) Confronting the invisible: assignment of protein $^{1}H^{N}$ chemical shifts in cases of extreme broadening. J Phys Chem Lett 11:3384–3389. https://doi.org/10.1021/acs.jpclett.0c00747

Yamazaki T, Muhandiram R, Kay LE (1994) NMR experiments for the measurement of carbon relaxation properties in highly enriched, uniformly ^{13}C,^{15}N-labeled proteins: application to $^{13}C^{\alpha}$ carbons. J Am Chem Soc 116:8266–8278. https://doi.org/10.1021/ja00097a037

Ying J, Delaglio F, Torchia DA, Bax A (2017) Sparse multidimensional iterative lineshape-enhanced (SMILE) reconstruction of both non-uniformly sampled and conventional NMR data. J Biomol NMR 68:101–118. https://doi.org/10.1007/s10858-016-0072-7

Yu B, Pletka CC, Pettitt BM, Iwahara J (2021) De novo determination of near-surface electrostatic potentials by NMR. Proc Natl Acad Sci 118:e2104020118. https://doi.org/10.1073/pnas.2104020118

Yu B, Pletka CC, Iwahara J (2022) Protein electrostatics investigated through paramagnetic NMR for nonpolar groups. J Phys Chem B 126:2196–2202. https://doi.org/10.1021/acs.jpcb.1c10930

Yuwen T, Sekhar A, Kay LE (2016) Evaluating the influence of initial magnetization conditions on extracted exchange parameters in NMR relaxation experiments: applications to CPMG and CEST. J Biomol NMR 65:143–156. https://doi.org/10.1007/s10858-016-0045-x